Geophysical Research Letters

RESEARCH LETTER
10.1029/2020GL092198

New Constraints on the Lunar Optical Space Weathering Rate

C. J. Tai Udovicic[1], E. S. Costello[2], R. R. Ghent[3], and C. S. Edwards[1]

[1]Northern Arizona University, Flagstaff, AZ, USA, [2]University of Hawai'i at Manoa, Honolulu, HI, USA, [3]Planetary Science Institute, Tucson, AZ, USA

Key Points:

- We model nanophase and microphase iron accumulation rates using published parameter maps and crater ages
- Highlands nanophase iron is negligible at 100 ka and accumulates at ~0.05 wt% ln (Ma)$^{-1}$ until ~1 Ga
- Highlands microphase iron is enhanced by 100 ka and less correlated with age, possibly due to variable abundances in lunar source materials

Supporting Information:

Supporting Information may be found in the online version of this article.

Correspondence to:

C. J. Tai Udovicic,
cjtu@nau.edu

Citation:

Tai Udovicic, C. J., Costello, E. S., Ghent, R. R., & Edwards, C. S. (2021). New constraints on the lunar optical space weathering rate. *Geophysical Research Letters*, *48*, e2020GL092198. https://doi.org/10.1029/2020GL092198

Received 17 DEC 2020
Accepted 4 JUN 2021

Abstract Space weathering processes form submicroscopic metallic iron particles that are optically active, darkening and reddening the lunar surface over time. The optical effects of these particles depend on their size; nanophase iron darkens and reddens, while microphase iron darkens without reddening. Using available Kaguya Multiband Imager parameter maps believed to estimate submicroscopic iron abundance, we investigate trends that may be associated with abundance of nanophase and microphase iron near dated lunar craters. We observe that nanophase iron is strongly correlated with crater age, while microphase iron exhibits a weaker correlation. We present models for the highlands nanophase and microphase iron accumulation rates from 100 ka to 1 Ga. Our observations suggest that highlands nanophase iron abundance is a direct result of space weathering exposure, while highlands microphase iron abundance is likely influenced by lunar source materials or stochastic impact-delivery mechanisms.

Plain Language Summary The Moon, Mercury, and asteroids lack protective atmospheres and slowly darken over time due to their exposure to space. We call this darkening process space weathering. Apollo samples returned from the Moon show that space weathering produces tiny iron particles that range in size from nanometers to micrometers. We use orbital lunar maps of nanophase and microphase iron content to better understand how quickly space weathering occurs on the Moon. We first find the iron content of young lunar soils deposited by large impact events, then use the age of each impact crater to see how much iron accumulates in different lengths of time. We find that nanophase iron accumulates predictably over time due to space weathering. In contrast, microphase iron accumulates less predictably, possibly because it exists in the lunar soil initially, or is delivered to the Moon by crater-forming impacts. This work helps us understand how the surface of the Moon weathers over time and how space weathering might work elsewhere in the Solar System.

1. Introduction

Space weathering is the combination of processes that physically and chemically alter the surfaces of airless bodies over time. On the Moon, space weathering darkens and reddens the optical spectrum through formation of fine metallic iron particles, termed submicroscopic iron (smFe^0; Cassidy & Hapke, 1975; Hapke, 2001; Pieters et al., 2000). The optical effects of smFe^0 are highly dependent on its size: smaller nanophase iron particles (1–40 nm) cause optical darkening and reddening, and larger microphase iron particles (40 nm–2 μm, sometimes called Britt-Pieters particles) darken without reddening (Britt & Pieters, 1994; Keller & Clemett, 2001; Lucey & Noble, 2008; Lucey & Riner, 2011; Noble et al., 2007). In this work, we use published parameter maps thought to represent different forms of smFe^0 along with craters of known age to estimate the rate of accumulation of nanophase and microphase iron on the lunar surface.

Several mechanisms of smFe^0 formation are actively debated in the literature. An early hypothesis suggested that solar wind sputtering and/or H^+ implantation could reduce mineral iron in oxides (FeO) to form metallic Fe^0 (Cassidy & Hapke, 1975; Wehner, 1961). While ion irradiation experiments are capable of producing smFe^0, it appears that H^+ implantation is not a necessary precursor as seen in He ion irradiation and pulse laser experiments which simulate micrometeorite bombardment (Loeffler et al., 2009; Sasaki et al., 2001). The discovery of thin smFe^0-bearing rims on individual regolith grains appeared to solve the conundrum (Keller & McKay, 1993, 1997). Hapke (2001) described a model by which solar wind sputtered and micrometeorite vaporized material would naturally deposit nanophase iron on adjacent grains (Hapke, 1973). The smFe^0-bearing grain rims could then combine and form the full distribution of nanophase and microphase

iron particles found in agglutinates by successive melt/vaporization events (Noble et al., 2007; Pieters & Noble, 2016). The sputter deposit aspect of this model is backed by several remote observations that report reduced optical space weathering in zones of reduced solar wind flux (e.g., at higher latitude or on magnetically shielded lunar swirls; Glotch et al., 2015; Hemingway et al., 2015; Sim et al., 2017). Thus far, laboratory simulations of solar wind irradiation have failed to confirm the solar wind sputter-deposits (Christoffersen et al., 2015). In addition, solar wind contribution is called into question by immature Apollo soils which appear to contain an abundance of nanophase iron in micrometeorite-associated vapor deposits, relative to solar-wind damaged grain rims (Keller & Zhang, 2015). Here, we provide new constraints on the possible $smFe^0$ formation mechanisms by leveraging modeled nanophase and microphase iron particle abundances predicted from radiative-transfer modeling (Trang & Lucey, 2019).

While most of the lunar surface is heavily space weathered and locally homogenized by regolith gardening, notable exceptions are the bright rays and youthful ejecta of recently formed craters. Impact craters provide natural time stamps on the lunar surface and their ejecta have informed our understanding of lunar space weathering for decades (e.g., Grier et al., 2001; Shoemaker & Hackman, 1962). Notably, the Diviner rock abundance proximal to dated craters exhibits a tight correlation with crater age, constraining the mechanical weathering of surface rocks and providing a new chronometer used to date similarly rocky craters (Ghent et al., 2014; Mazrouei et al., 2019). Constraining the optical weathering rate of the regolith has proven more challenging, partially due to target composition biasing optical maturity parameters, inhibiting global comparisons (Braden & Robinson, 2013; Grier et al., 2001; Nettles et al., 2011).

This work updates our understanding of the optical weathering rate in two important ways. First, we use modern parameter maps of nanophase and microphase iron which are empirically validated by Apollo soil spectra and backed by a physical radiative-transfer model (Trang & Lucey, 2019). Second, we use a larger sample of dated lunar craters <1 Ga, enabled by recent developments in remote detection and chronology of young lunar craters (Ghent et al., 2014; Williams et al., 2018). For comparison with previous work, we apply our methodology to a database of large rayed craters previously investigated with the Clementine optical maturity parameter (Grier et al., 2001). We present new surface accumulation rates of nanophase and microphase iron and discuss key constraints that they place on the lunar optical space weathering rate.

2. Methods

We split our analysis into 2 parts: Global and Highlands. First, we investigate global (within ±60° latitude) $smFe^0$ trends, incorporating both the highlands and mare regions. Using crater populations dated relative to one another, we present overall trends in the nanophase and microphase iron with age and show heritage from the Grier et al. (2001) global study of lunar optical maturity (Figure 2). Second, we restrict our study to the lunar highlands and craters with absolute model ages. We derive surface accumulation rates from time-resolved fits to the highlands nanophase and microphase iron abundance (Figure 3). This portion of the analysis is limited to the iron-poor lunar highlands which are more consistent in FeO content and optical space weathering trends (Lucey et al., 1998; McFadden et al., 2019; Trang & Lucey, 2019).

2.1. Nanophase and Microphase Iron Abundance

We define an annular region of interest around each crater in the global 60°N–60°S, 1 km/pixel nanophase and microphase iron maps of Trang and Lucey (2019) using the craterpy Python package (Tai Udovicic, 2021). We scale each annulus with crater radius; the inner edge of the annulus is set at the crater rim (one crater radius from the center), while the outer edge of the annulus extends to four crater radii (Figure 1). We parameterize each crater by the mean nanophase and mean microphase iron abundance within the annulus, excluding terrain within the crater rim which may be refreshed by mass wasting on steep slopes. In the global analysis, the mean iron abundances are grouped by relative age (Figure 2). In the highlands analysis, the mean iron abundances of each crater are plotted with age (Figure 3).

Four crater radii is chosen as the maximum annular extent because the youngest craters in our sample typically feature a continuous nanophase iron depletion zone of this size. We note that a small fraction (~9%) of our highlands crater population exhibit asymmetric ejecta, causing some background contamination in select craters (e.g., Cold Spot 3, Figure 1). In addition, small fresh impacts may act to refresh the material

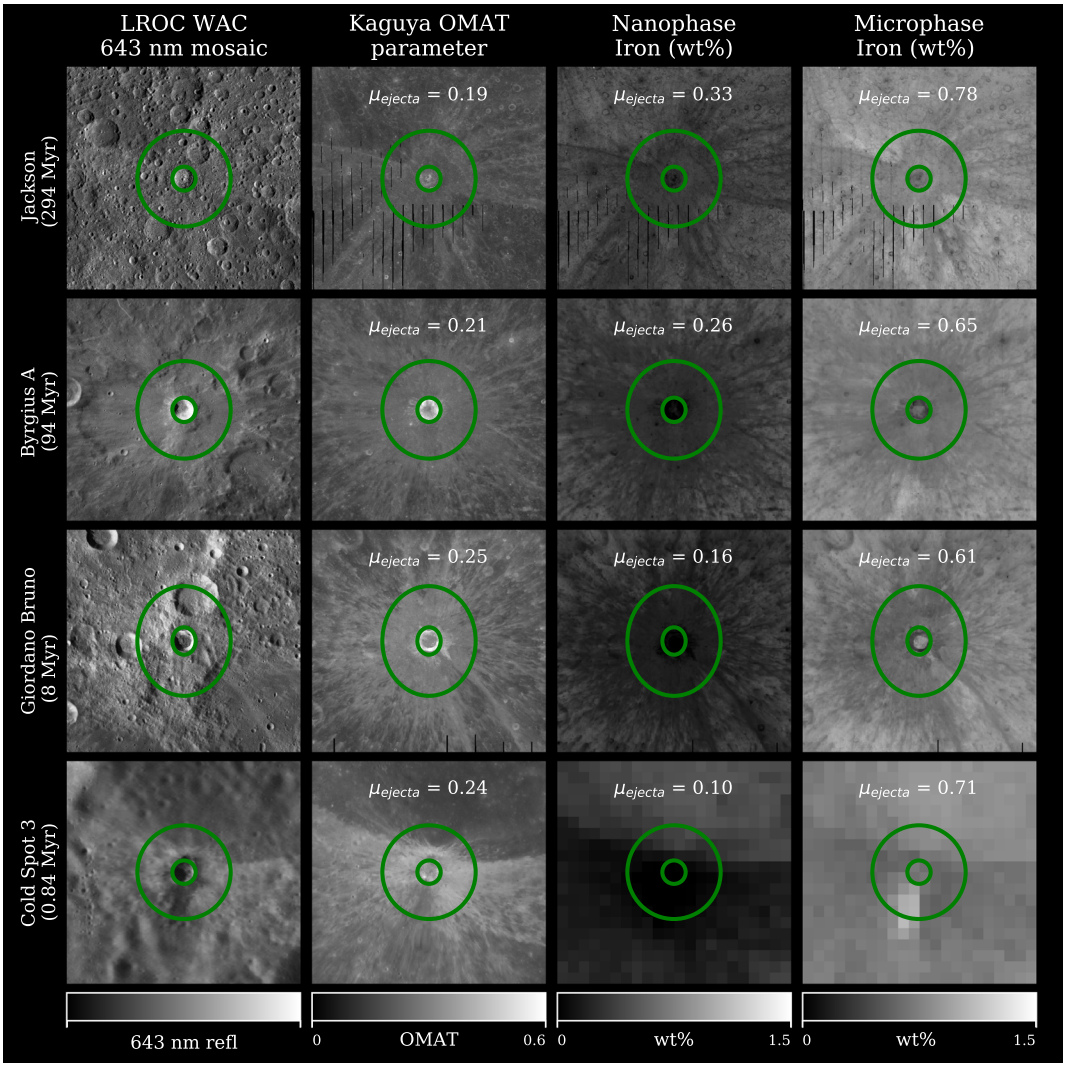

Figure 1. Four craters of decreasing model age (descending order) shown in the Lunar Reconnaissance Orbiter Wide Angled Camera 643 nm mosaic, Kaguya OMAT parameter, nanophase iron abundance, and microphase iron abundance (left to right; Lemelin et al., 2016; Speyerer et al., 2011; Trang & Lucey, 2019). Ejecta annuli extending from each crater rim to 4 crater radii are denoted in green. Mean OMAT, nanophase iron abundance, and microphase iron abundance computed within the annulus are shown in each respective inset as μ_{ejecta}.

within our chosen annulus. We limit our sample to craters of sufficient size (annulus ≥ 12 pixels) such that these effects are minor for any given crater (Figure S3). Additionally, we fit a sufficient sample ($n = 77$ craters in the highlands) such that these effects are negligible on our overall trends (Figure S4). We do not undertake a detailed mapping of crater ejecta because anomaly identification is likely to be biased for craters near the resolution limit of the Trang and Lucey (2019) maps.

2.2. Crater Populations

The global analysis uses two published crater databases providing relative crater ages. The LPI crater database consists of the 421 craters dated as Copernican, Eratosthenian, and Imbrian in the Lunar and Planetary Institute Lunar Impact Crater Database (Losiak et al., 2015). The OMAT crater database contains large rayed craters relatively dated by Grier et al. (2001) as Young (appear younger than Tycho), Intermediate (appear younger than Copernicus) and Old (appear older than Copernicus) using the Clementine Optical Maturity (OMAT) parameter (Table 1).

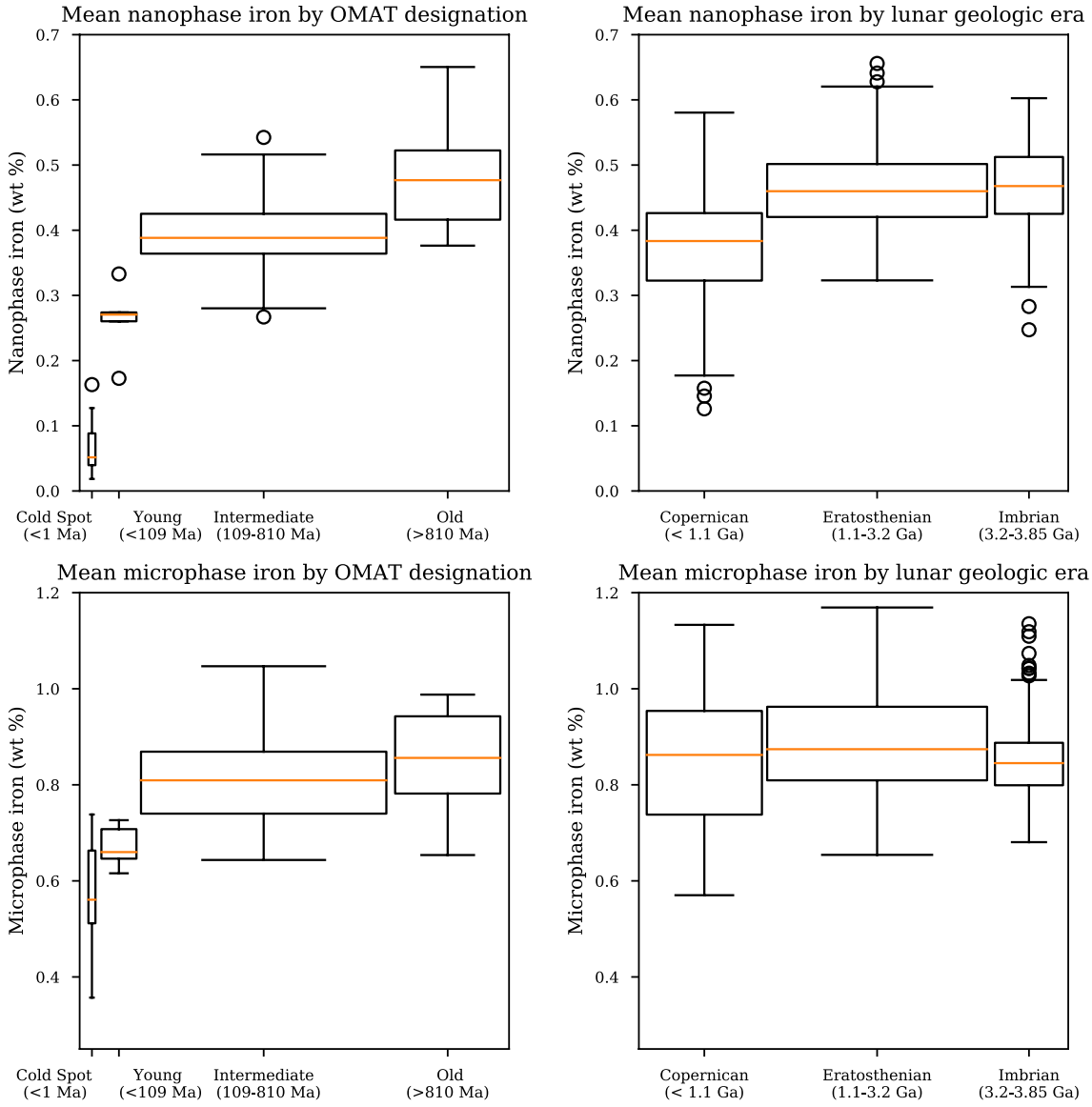

Figure 2. Box plots of global mean nanophase iron (top) and microphase iron (bottom) in the crater annuli of the OMAT (left) and LPI databases (right), grouped by relative age. Cold spot craters are included as a young endmember population. The central orange bar of each population denotes the median and the whiskers denote 1.5*IQR (interquartile range). Circles denote outliers outside 1.5*IQR. Nanophase and microphase iron abundances increase with relative ages of OMAT craters. Copernican craters exhibit a paucity of nanophase iron relative to Eraotsthenian and Imbrian craters, but this contrast is less apparent for microphase iron.

The highlands analysis uses three published crater databases providing absolute model ages of craters. The Chronology crater database consists of eight craters dated using crater counting techniques, assuming the standard lunar chronology function (e.g., Neukum et al., 2001). These craters are Byrgius A, Giordano Bruno, Hell Q, Jackson, King, Moore F, Necho, and Tycho (Ashley et al., 2012; Eugster, 1999; Hiesinger et al., 2012; Morota et al., 2009; Salih et al., 2016; van der Bogert et al., 2010). For craters with multiple published ages, we selected model ages derived from crater counts on the ejecta.

The Rock Abundance crater database consists of 57 craters ≥10 km in diameter which have published absolute model ages based on the Diviner Rock Abundance of their ejecta (Ghent et al., 2014; Mazrouei et al., 2019). Several Chronology craters are duplicated in the Rock Abundance database. Where this is the case, we choose the model age predicted by the standard lunar chronology function.

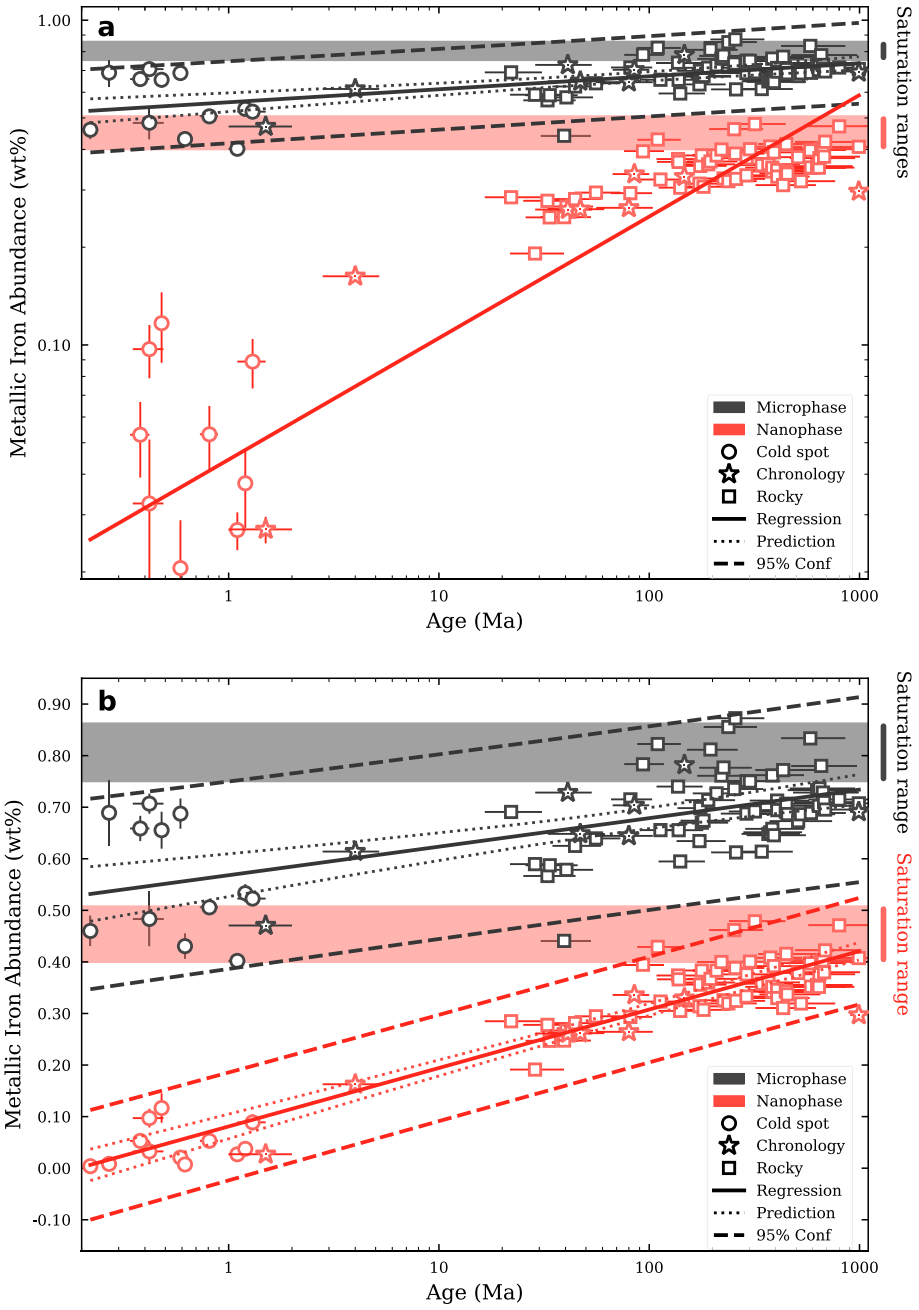

Figure 3. Mean abundances of highlands microphase iron (black) and nanophase iron (red) in crater annuli plotted over crater age. (a) Log-log axes and straight-line power law fits. (b) Linear-log axes and straight-line linear-logarithmic fits. Saturation ranges (shaded regions) denote the mean $\pm 1\sigma$ of non-Copernican highlands LPI craters. Ordinary least squares regression fits (Equations 1–3), prediction intervals and 95% confidence intervals are shown.

The Cold Spot crater database consists of 12 Diviner cold spot craters dated by crater counting techniques and the standard lunar chronology function (Williams et al., 2018). We group this database separately from the Chronology craters because they form a population of the youngest craters in our sample and are thermophysically distinct (Williams et al., 2018).

The Highlands Saturation Range population consists of 52 craters used to infer the levels of saturation for the nanophase and microphase iron in the lunar highlands. This population is a subset of the LPI crater database containing only highlands craters Eratosthenian or older and ≤200 km in diameter.

Table 1
The Five Impact Crater Databases, the Ages They Provide, and the Final Counts Used in This Study (see Data Sets S1 & S2 for Full Tables)

Crater database	Age classification	Population age	Count
Cold spot[a]	Absolute	220 ka–1.3 Ma	12
Chronology[a]	Absolute	1.5 Ma–990 Ma	8
Rock abundance[a]	Absolute	22 Ma–990 Ma	57
OMAT	Young	≤Tycho (∼100 Ma)	5
	Intermediate	Tycho – Copernicus	38
	Old	>Copernicus (∼800 Ma)	18
LPI	Copernican	<1.1 Ga	70
	Eratosthenian	1.1 Ga–3.2 Ga	118
	Imbrian	3.2 Ga–3.85 Ga	233
Saturation range[a]	≥Eratosthenian	≥1.1 Ga	52

[a]Highlands subset only

We filter all craters by the following criteria: The entire ejecta annulus falls in bounds of, and represents at least 12 pixels in, the 1 km/pixel, 60°N, 60°S global $smFe^0$ maps (Trang & Lucey, 2019). Highlands crater annuli must additionally not cross the mare bounds defined by Nelson et al. (2014), who used Lunar Reconnaissance Orbiter Camera (LROC) images to precisely demarcate lunar mare boundaries. Although the $smFe^0$ maps decrease in mean abundance at latitudes pole-wards of ±50° (Trang & Lucey, 2019), all dated highlands craters that meet the above criteria are within 50°N and 50°S so we do not apply a latitude correction in this work (Figure S1).

Final counts and age summaries for each database are given in Table 1. See Data Sets S1 and S2 for full crater lists and derived $smFe^0$ abundances.

3. Results

3.1. Global Analysis

We plot our derived distribution of mean nanophase and microphase iron for craters from the LPI and OMAT databases, grouped by relative age (Figure 2). The Cold Spot database is included as the young endmember population for comparison. We observe consistently lower modeled nanophase iron abundance relative to microphase iron. Unexpectedly, microphase iron is enhanced (median > 0.5 wt %) initially for cold spot craters (≤1 Ma), while nanophase iron is negligible for the same craters (median < 0.05 wt %). In the LPI populations, only the Copernican range exhibits reduced nanophase and microphase iron, consistent with having observable unsaturated rays (Losiak et al., 2015; Shoemaker & Hackman, 1962). No significant $smFe^0$ variation is observed in non-Copernican populations (i.e., OMAT Old, Eratosthenian, and Imbrian craters), implying saturation. Relatively wide saturation ranges are expected due to variable FeO content in the mare and highlands, as discussed in Trang and Lucey (2019). In addition, we observe that nanophase iron abundance is consistently lower than microphase iron abundance across all populations, while the former appears to increase rapidly on very young surfaces.

3.2. Highlands Analysis

We plot the mean nanophase and microphase iron of each highlands crater versus crater age (Figure 3). Age uncertainties indicated are the crater chronology model age uncertainties for Cold Spot and Chronology craters, and the 95% credible intervals for Rock Abundance craters (see references in Table 1). Uncertainties in $smFe^0$ are the standard error of the mean within each crater annulus. To investigate the evolution of $smFe^0$ over time, we plot these data both on log-log and linear-log axes (Figures 3a and 3b, respectively).

Linear fits on log-log axes are consistent with power law growth in time (Figure 3a). Microphase iron appears weakly power-law correlated ($R^2 = 0.37$, Equation 1). By contrast, nanophase iron is non-linear on log-log axes, indicating non-power law growth (more apparent on linear axes (Figure S2).

Linear fits on linear-log axes are consistent with logarithmic functions of time (Figure 3b). The logarithmic fit to microphase iron is again weakly correlated ($R^2 = 0.36$), while nanophase iron is strongly correlated in log-time ($R^2 = 0.88$). Logarithmic fits predict a greater y-intercept (early abundance) for microphase iron ($a = 0.57$ wt%, b: 0.024), relative to ($a = 0.081$ wt%, b: 0.049) for nanophase iron, where fits are given by $y = a + b\log(x)$ (Equations 2 and 3). We discuss the significance of the differing intercepts in Section 4.2.

We also compute saturation ranges of nanophase iron (0.40–0.51 wt%) and microphase iron (0.75–0.86 wt%) representing the mean $\pm 1\sigma$ range of $smFe^0$ in LPI Highlands Saturation annuli (shaded regions, Figure 3). The fits described above and in Equations 1–3 each reach saturation in 1 Ga within error, as expected.

We note that the power law and logarithmic fits for microphase iron are equivalent within error, but we present both fits for ease of comparison with previous power law models of space weathering and impact

flux (e.g., Ghent et al., 2014; Mazrouei et al., 2019). The power law curve of best fit (Figure 3a) is given below, where y is microphase iron abundance (wt%) and x is age (Ma).

$$y_{\text{microphase}} = (0.56 \pm 1)x^{0.040\pm0.0059},\ R^2 = 0.37 \quad (1)$$

The logarithmic curves of best fit of microphase and nanophase iron (Figure 3b) are given below, where y is metallic iron abundance (wt%) and x is age (Ma).

$$y_{\text{microphase}} = (0.57 \pm 0.018) + (0.024 \pm 0.0037)\log(x),\ R^2 = 0.36 \quad (2)$$

$$y_{\text{nanophase}} = (0.081 \pm 0.010) + (0.049 \pm 0.0021)\log(x),\ R^2 = 0.88 \quad (3)$$

In summary, our results place the following empirical constraints on the growth of highlands nanophase and microphase iron over time.

1. Both nanophase and microphase iron are correlated in logarithmic time.
2. Microphase iron is less correlated than nanophase iron in log-time ($R^2 = 0.36$ and $R^2 = 0.88$, respectively).
3. Nanophase iron is negligible initially (0 wt% within error for craters 100 ka or younger).
4. Microphase iron appears to be elevated initially or very soon after crater formation (~0.5 wt% for 100 ka craters).

4. Discussion

4.1. Global Constraints

We observe clear increasing trends in absolute nanophase and microphase iron abundance over Copernican timescales (Figure 2). Both sizes of $smFe^0$ appear saturated for non-Copernican populations (i.e., OMAT old, Eratosthenian, and Imbrian), as expected. The greater abundance of microphase iron relative to nanophase iron, particularly in the youngest craters, is notable and will be discussed further below. Our analysis shows that previous crater maturity studies with OMAT are broadly consistent with the modeled nanophase and microphase iron abundances of Trang and Lucey (2019). Further global interpretations would require a more detailed understanding of how local iron composition influences the rate of production and saturation limits of $smFe^0$ (McFadden et al., 2019; Trang & Lucey, 2019).

4.2. Highlands Constraints

Our modeled linear-logarithmic fit to highlands nanophase iron abundance exhibits a strong correlation with age ($R^2 = 0.88$) and an approach to saturation in ~1 Ga, that is, on a Copernican timescale, as expected (Equation 2; Figure 3b). Our model residuals are consistent with respect to latitude, longitude, crater radius, and crater age, suggesting the trend we observe is robust (Figure S5). Our model also predicts negligible nanophase iron in the initial primary ejecta of craters in our sample (>0.5 km diameter). Our results are consistent with ferromagnetic resonance (FMR) measurements of $smFe^0$ in Apollo soils which found that nanophase iron is strongly correlated with maturity and negligible in pristine regolith (Morris, 1980). Our model is broadly consistent with our understanding of lunar space weathering and relates modeled nanophase iron abundance to surface exposure age for the first time.

In contrast, highlands microphase iron exhibits weakly correlated linear-logarithmic or power law growth over time ($R^2 = 0.36$ and 0.37, respectively). Since these fits are indistinguishable within errors, we discuss the linear-logarithmic model which is both simpler and consistent with the nanophase iron model. The non-zero early abundance and weak correlation of microphase iron with crater age are qualitatively similar to the trends Morris (1980) identified in Apollo samples. That study found that the microphase fraction of $smFe^0$ is present in pristine Apollo soils and is weakly correlated with maturity, likely due to the variable quantities present in lunar source materials. We note that our modeled microphase iron abundance saturation range (0.75–0.86 wt%) exceeds the maximum corresponding Fe^0_C–Fe^0_A content (0.56 wt %) measured

by Morris (1980). This discrepancy could be due to the Trang and Lucey (2019) radiative-transfer model assuming microphase iron particles are ≥33 nm, smaller than other derivations of the microphase iron particle size in the literature (Lucey & Riner, 2011; Noble et al., 2007). If the microphase iron particle size is increased in the Trang and Lucey (2019) model, we would expect an overall downward shift in microphase iron abundances that would preserve the trends we observe over time. Therefore, the microphase iron models we present in Equations 1 and 2 capture trends in the relative abundance of microphase iron over time, though they may not be reliable as absolute wt % abundance predictors.

4.3. A Broken Link Between Nanophase and Microphase Iron Accumulation

Our analysis of highlands $smFe^0$ reveals three primary differences in the accumulation of nanophase and microphase iron over 100 ka–1 Ga:

1. Crater ejecta ~100 ka contain negligible nanophase iron, but detectable microphase iron.
2. Microphase iron is less correlated with crater age than nanophase iron.
3. Nanophase iron accumulates at a greater rate (steeper log slope) than microphase iron through time.

We discuss the implications of these constraints on the following models of optical space weathering:

Nanophase aggregation: A common hypothesis is that nanophase iron is primarily formed in vapor deposits by micrometeorite impacts and is later aggregated to form microphase iron in agglutinates (Pieters & Noble, 2016). This hypothesis is corroborated by the observation that nanophase iron is found primarily in the rims of individual soil particles, while microphase iron is found in heavily reworked agglutinates (Keller & Clemett, 2001; Keller & McKay, 1993, 1997).

Our observations indicate that if nanophase aggregation is the primary space weathering mechanism, then either the Trang and Lucey (2019) maps preferentially overestimate the abundance of microphase iron near young craters, or the provenance of microphase iron abundance is more linked to source materials than space weathering products. From 100 ka until saturation, microphase iron is much more weakly correlated with crater age ($R^2 = 0.36$) than nanophase iron ($R^2 = 0.88$), indicating that microphase iron abundance is only a minor function of exposure to space weathering. This observation could be explained if highlands source materials (e.g., bedrock and breccia) contain highly variable quantities of microphase iron, thus seeding each crater in our sample with an independent initial abundance. Additionally, Morris (1980) also proposed that impactors larger than micrometeorites may be a source of microphase iron. If this is the case, the initial quantity of microphase iron could also depend on the composition of the primary impactor, while delivery of microphase iron by later non-micrometeorite impacts may explain the variance in our observations. Therefore, while micrometeorite bombardment may aggregate nanophase iron into microphase iron, our observations suggest this is not the primary source of microphase iron in the highlands regolith.

Nanophase and microphase independent growth: An alternative hypothesis is that nanophase and microphase iron accumulation are governed by independent processes. For example, solar wind and micrometeorites could both play significant but distinct roles in lunar space weathering. This hypothesis is most commonly supported by observations of inconsistent weathering trends correlated with the solar wind flux, for example, with latitude, across magnetic anomalies, and on equator-ward and pole-ward facing slopes (Glotch et al., 2015; Hemingway et al., 2015; Sim et al., 2017).

Our observations are consistent with a mechanism by which nanophase iron accumulation is controlled by the solar wind while microphase iron accumulation is controlled by micrometeorites (Hemingway et al., 2015). Observations of Apollo soils have revealed that solar wind amorphized rims in the finest fraction of lunar soil grow in thickness over logarithmic time, while vapor deposited rim thicknesses show no correlation in time (Keller & Zhang, 2015). The logarithmic growth of solar wind amorphized rims of the finest fraction of lunar soil may suggest that the well-correlated logarithmic growth of nanophase iron we observe here is controlled by solar wind amorphization of the finest fraction. Micrometeorites may then be responsible for redistributing solar wind-produced nanophase iron in depositional rims and/or aggregating it into microphase iron in agglutinates, as described above. Alternatively, microphase iron growth may be controlled entirely by micrometeorite or larger impactors with negligible input from the solar wind, as the saturation of lunar swirls in microphase — but not nanophase — iron appears to suggest (Trang

& Lucey, 2019). The potential bombardment source of microphase iron in Apollo soils was noted to be indistinguishable from lunar source materials by Morris (1980). Similarly, our analysis cannot distinguish between microphase iron present initially in lunar highlands materials or delivered stochastically by later bombardment.

The nanophase and microphase iron accumulation rates we present are broadly consistent with our understanding of lunar space weathering. Our results also suggest that parameterizing crater ejecta by the mean within four crater radii is a simple yet effective tool for comparing crater ejecta across orders of magnitude in size and age. Extending these analyses to the lunar maria could further constrain the role of source materials in the accumulation of nanophase and microphase iron on the lunar surface, in turn yielding additional insights for the role of solar wind and micrometeorites in lunar space weathering. We also note that while the final saturation of nanophase and microphase iron is likely governed by gradual homogenization by impact gardening (Costello et al., 2018; Gault et al., 1974), we find no significant change in linear-log accumulation rate of $smFe^0$ over the crater ages and sizes observed here.

5. Conclusions

Our analysis reveals distinctions between the surface accumulation of nanophase iron and microphase iron over time on the lunar surface. Globally, the nanophase and microphase iron parameters accumulate over time and show good agreement with prior investigations of optical space weathering. In the lunar highlands, we observe negligible nanophase iron <100 ka and a tightly correlated accumulation from 100 ka to 1 Ga. By contrast, we observe an initial enhancement in microphase iron associated with very young craters <100 ka, followed by a gradual approach to saturation from 100 ka to 1 Ga. For the first time, we present quantitative accumulation rates of lunar nanophase and microphase iron in the highlands. Furthermore, our analyses suggest that space weathering exposure is the primary predictor of highlands nanophase iron abundance, while highlands microphase iron abundance may be more heavily influenced by lunar source materials or delivery by micrometeorite or larger impacts. The insights into lunar $smFe^0$ presented here will help disentangle the myriad processes that weather the surfaces of airless bodies over time.

Data Availability Statement

The space weathering data used in this study are publicly available via the Geosciences Node of the Planetary Data System: https://pds-geosciences.wustl.edu/missions/kaguya/trang_moon.htm. Python code used to extract regions of interest from these data is available via the open source Craterpy (Version 0.5.1) Python package which is available for use with proper citation under the MIT license (DOI: https://doi.org/10.5281/zenodo.830057). Current versions of craterpy are also available from the GitHub repository: https://github.com/cjtu/craterpy. Crater data tables produced in this work are described in the supplementary information and are available for use with proper citation under the CC BY 4.0 license (DOI: https://doi.org/10.5281/zenodo.4345058).

Acknowledgments
The authors would like to thank C. M. Pieters and an anonymous reviewer for their helpful comments which greatly improved this work.

References

Ashley, J. W., Robinson, M. S., Hawke, B. R., Van Der Bogert, C. H., Hiesinger, H., Sato, H., et al. (2012). Geology of the king crater region: New insights into impact melt dynamics on the Moon. *Journal of Geophysical Research: Planets*, *117*(E12). https://doi.org/10.1029/2011je003990

Braden, S. E., & Robinson, M. S. (2013). Relative rates of optical maturation of regolith on Mercury and the Moon. *Journal of Geophysical Research: Plan*, *118*(9), 1903–1914. https://doi.org/10.1002/jgre.20143

Britt, D. T., & Pieters, C. M. (1994). Darkening in black and gas-rich ordinary chondrites: The spectral effects of opaque morphology and distribution. *Geochimica et Cosmochimica Acta*, *58*(18), 3905–3919. https://doi.org/10.1016/0016-7037(94)90370-0

Cassidy, W., & Hapke, B. (1975). Effects of darkening processes on surfaces of airless bodies. *Icarus*, *25*(3), 371–383. https://doi.org/10.1016/0019-1035(75)90002-0

Christoffersen, R., Dukes, C., Keller, L., Rahman, Z., & Baragiola, R. (2015). Problems at the Leading edge of space weathering as revealed by TEM combined with surface science techniques. Space Weathering of Airless Bodies: An Integration of Remote Sensing Data, Laboratory Experiments and Sample Analysis Workshop (Vol. 1878, pp. 2065). Lunar and Planetary Institute. https://www.hou.usra.edu/meetings/airlessbodies2015/pdf/2065.pdf

Costello, E. S., Ghent, R. R., & Lucey, P. G. (2018). The mixing of lunar regolith: Vital updates to a canonical model. *Icarus*, *314*, 327–344. https://doi.org/10.1016/j.icarus.2018.05.023

Eugster, O. (1999). Chronology of dimict breccias and the age of South Ray crater at the Apollo 16 site. *Meteoritics and Planetetary Science*, *34*(3), 385–391. https://doi.org/10.1111/j.1945-5100.1999.tb01347.x

Gault, D., Hörz, F., Brownlee, D., & Hartung, J. (1974). Mixing of the lunar regolith. *Lunar and planetary science conference proceedings*, *5*, 2365–2386.
Ghent, R. R., Hayne, P. O., Bandfield, J. L., Campbell, B. A., Allen, C. C., Carter, L. M., & Paige, D. A. (2014). Constraints on the recent rate of lunar ejecta breakdown and implications for crater ages. *Geology*, *42*(12), 1059–1062. https://doi.org/10.1130/g35926.1
Glotch, T. D., Bandfield, J. L., Lucey, P. G., Hayne, P. O., Greenhagen, B. T., Arnold, J. A., et al. (2015). Formation of lunar swirls by magnetic field standoff of the solar wind. *Nature Communications*, *6*, 6189. https://doi.org/10.1038/ncomms7189
Grier, J. A., McEwen, A. S., Lucey, P. G., Milazzo, M., & Strom, R. G. (2001). Optical maturity of ejecta from large rayed lunar craters. *Journal of Geophysical Research: Planets*, *106*(E12), 32847–32862. https://doi.org/10.1029/1999je001160
Hapke, B. (1973). Darkening of silicate rock powders by solar wind sputtering. *The Moon*, *7*(3–4), 342–355. https://doi.org/10.1007/bf00564639
Hapke, B. (2001). Space weathering from Mercury to the asteroid belt. *Journal of Geophysical Research: Plan*, *106*(E5), 10039–10073. https://doi.org/10.1029/2000je001338
Hemingway, D., Garrick-Bethell, I., & Kreslavsky, M. (2015). Latitudinal variation in spectral properties of the lunar maria and implications for space weathering. *Icarus*, *261*, 66–79. https://doi.org/10.1016/j.icarus.2015.08.004
Hiesinger, H., Van Der Bogert, C. H., Pasckert, J. H., Funcke, L., Giacomini, L., Ostrach, L. R., & Robinson, M. S. (2012). How old are young lunar craters? *Journal of Geophysical Research: Planets*, *117*(E12). https://doi.org/10.1029/2011je003935
Keller, L. P., & Clemett, S. (2001). Formation of nanophase iron in the lunar regolith. *Lunar and planetary science conference*, 2097.
Keller, L. P., & McKay, D. S. (1993). Discovery of vapor deposits in the lunar regolith. *Science*, *261*(5126), 1305–1307. https://doi.org/10.1126/science.261.5126.1305
Keller, L. P., & McKay, D. S. (1997). The nature and origin of rims on lunar soil grains. *Geochimica et Cosmochimica Acta*, *61*(11), 2331–2341. https://doi.org/10.1016/s0016-7037(97)00085-9
Keller, L. P., & Zhang, S. (2015). Rates of space weathering in Lunar soils. *Laboratory Experiments and Sample Analysis Workshop*, *1878*, 2056.
Lemelin, M., Lucey, P., Gaddis, L., Hare, T., & Ohtake, M. (2016). Global map products from the Kaguya multiband imager at 512 ppd: Minerals, FEO, and OMAT. *Lunar and Planetary Science Conference*, 2994.
Loeffler, M., Dukes, C., & Baragiola, R. (2009). Irradiation of olivine by 4 keV He+: Simulation of space weathering by the solar wind. *Journal of Geophysical Research*, *114*(E3). https://doi.org/10.1029/2008je003249
Losiak, A., Wilhelms, D., Byrne, C., Thaisen, K., Weider, S., Kohout, T., et al. (2015). A new lunar impact crater database, In T., Ohman (Eds.), *40th Lunar and Planetary Science Conference*, *1532*. Retrieved from https://www.lpi.usra.edu/lunar/surface/Lunar\%5FImpact\%5FCrater\%5FDatabase\%5Fv08Sep2015.xls
Lucey, P. G., Blewett, D. T., & Hawke, B. R. (1998). Mapping the FeO and TiO2 content of the lunar surface with multispectral imagery. *Journal of Geophysical Research: Planets*, *103*(E2), 3679–3699. https://doi.org/10.1029/97je03019
Lucey, P. G., & Noble, S. K. (2008). Experimental test of a radiative transfer model of the optical effects of space weathering. *Icarus*, *197*(1), 348–353. https://doi.org/10.1016/j.icarus.2008.05.008
Lucey, P. G., & Riner, M. A. (2011). The optical effects of small iron particles that darken but do not redden: Evidence of intense space weathering on mercury. *Icarus*, *212*(2), 451–462. https://doi.org/10.1016/j.icarus.2011.01.022
Mazrouei, S., Ghent, R. R., Bottke, W. F., Parker, A. H., & Gernon, T. M. (2019). Earth and moon impact flux increased at the end of the paleozoic. *Science*, *363*(6424), 253–257. https://doi.org/10.1126/science.aar4058
McFadden, J., Garrick-Bethell, I., Sim, C. K., Kim, S. S., & Hemingway, D. (2019). Iron content determines how space weathering flux variations affect lunar soils. *Icarus*, *333*, 323–342. https://doi.org/10.1016/j.icarus.2019.05.033
Morota, T., Haruyama, J., Miyamoto, H., Honda, C., Ohtake, M., Yokota, Y., et al. (2009). Formation age of the lunar crater giordano bruno. *Meteoritics and Planetetary Science*, *44*(8), 1115–1120. https://doi.org/10.1111/j.1945-5100.2009.tb01211.x
Morris, R. V. (1980). Origins and size distribution of metallic iron particles in the lunar regolith. *Lunar and planetary science conference*, *2*, 1697–1712.
Nelson, D. M., Koeber, S. D., Daud, K., Robinson, M. S., Watters, T., Banks, M., & Williams, N. R. (2014). Mapping lunar maria extents and lobate scarps using lroc image products. *Lunar and planetary science conference*, 2861. Retrieved from http://www.hou.usra.edu/meetings/lpsc2014/pdf/2861.pdf
Nettles, J., Staid, M., Besse, S., Boardman, J., Clark, R., Dhingra, D., et al. (2011). Optical maturity variation in lunar spectra as measured by moon mineralogy mapper data. *Journal of Geophysical Research*, *116*. https://doi.org/10.1029/2010je003748
Neukum, G., Ivanov, B. A., & Hartmann, W. K. (2001). Cratering records in the inner solar system in relation to the lunar reference system. In *Chronology and evolution of mars* (pp. 55–86). Springer. https://doi.org/10.1007/978-94-017-1035-0_3
Noble, S. K., Pieters, C. M., & Keller, L. P. (2007). An experimental approach to understanding the optical effects of space weathering. *Icarus*, *192*(2), 629–642. https://doi.org/10.1016/j.icarus.2007.07.021
Pieters, C. M., & Noble, S. K. (2016). Space weathering on airless bodies. *Journal of Geophysical Research: Planets*, *121*(10), 1865–1884. https://doi.org/10.1002/2016je005128
Pieters, C. M., Taylor, L. A., Noble, S. K., Keller, L. P., Hapke, B., Morris, R. V., et al. (2000). Space weathering on airless bodies: Resolving a mystery with lunar samples. *Meteoritics and Planetary Science*, *35*, 1101–1107. https://doi.org/10.1111/j.1945-5100.2000.tb01496.x
Salih, A. L., Grumpe, A., Wöhler, C., & Hiesinger, H. (2016). Construction of an age map of the region around the young lunar crater Hell Q. *International Journal of Simulation Systems, Science, and Technology*, *17*, 33. https://doi.org/10.5013/IJSSST.a.17.33.59
Sasaki, S., Nakamura, K., Hamabe, Y., Kurahashi, E., & Hiroi, T. (2001). Production of iron nanoparticles by laser irradiation in a simulation of lunar-like space weathering. *Nature*, *410*(6828), 555–557. https://doi.org/10.1038/35069013
Shoemaker, E. M., & Hackman, R. J. (1962). Stratigraphic basis for a lunar time scale. In Z. Kopal & Z. K. Mikhailov (Eds.), *Symposium - International Astronomical Union*, *14*, 289–300. https://doi.org/10.1017/s007418090017826x
Sim, C. K., Kim, S. S., Lucey, P. G., Garrick-Bethell, I., & Choi, Y. J. (2017). Asymmetric space weathering on lunar crater walls. *Geophysical Research Letters*, *44*(22), 11273–11281. https://doi.org/10.1002/2017gl075338
Speyerer, E., Robinson, M., & Denevi, B. (2011). Lunar reconnaissance orbiter camera global morphological map of the moon. *Lunar and planetary science conference*, 2387.
Tai Udovicic, C. J. (2021). *Craterpy*. https://doi.org/10.5281/zenodo.4780769
Trang, D., & Lucey, P. G. (2019). Improved space weathering maps of the lunar surface through radiative transfer modeling of kaguya multiband imager data. *Icarus*, *321*, 307–323. https://doi.org/10.1016/j.icarus.2018.11.014

van der Bogert, C. H., Hiesinger, H., McEwen, A. S., Dundas, C., Bray, V., Robinson, M. S., et al. (2010). Discrepancies between crater size-frequency distributions on ejecta and impact melt pools at lunar craters: An effect of differing target properties. *Lunar and planetary science conference*.

Wehner, G. (1961). Sputtering effects on the moon's surface. *ARS Journal*, *31*(3), 438–439. https://doi.org/10.2514/8.5498

Williams, J. P., Bandfield, J. L., Paige, D. A., Powell, T. M., Greenhagen, B. T., Taylor, S., et al. (2018). Lunar cold spots and crater production on the moon. *Journal of Geophysical Research: Planets*, *123*(9), 2380–2392. https://doi.org/10.1029/2018je005652